Monthly Notices
of the
ROYAL ASTRONOMICAL SOCIETY

MNRAS **491,** 1673–1689 (2020)
Advance Access publication 2019 October 31

doi:10.1093/mnras/stz3060

Development of a simulator of the SIMBIOSYS suite onboard the BepiColombo mission

A. Slemer,[1★] M. Zusi,[2] E. Simioni,[3] V. Da Deppo,[1,3] C. Re,[3] A. Lucchetti,[3] V. Della Corte,[2] G. Filacchione,[2] P. Palumbo,[2,4] F. Capaccioni,[2] M. T. Capria,[2] M. Amoroso,[5] R. Mugnuolo[5] and G. Cremonese[3]

[1]*CNR-IFN Padova, Via Trasea 7, I-35131 Padova, Italy*
[2]*INAF-IAPS, Via Fosso del Cavaliere 100, I-00133 Roma, Italy*
[3]*INAF-OAPD, Vicolo dell'Osservatorio 5, I-35122 Padova, Italy*
[4]*Università degli Studi di Napoli 'Parthenope', Dip. Scienze e Tecnologie, Via Amm. F. Acton, 38, I-80133 Napoli, Italy*
[5]*ASI, Via del Politecnico, I-00133 Roma, Italy*

Accepted 2019 October 28. Received 2019 October 25; in original form 2019 July 18

ABSTRACT

BepiColombo is the fifth cornerstone mission of the European Space Agency (ESA) dedicated to study the Mercury planet. The BepiColombo spacecraft comprises two science modules: the Mercury Planetary Orbiter (MPO) realized by ESA and the Mercury Magnetospheric Orbiter provided by the Japan Aerospace Exploration Agency. The MPO is composed by 11 instruments, including the 'Spectrometer and Imagers for MPO BepiColombo Integrated Observatory System' (SIMBIOSYS). The SIMBIOSYS suite includes three optical channels: a Stereoscopic Imaging Channel, a High Resolution Imaging Channel, and a Visible and near Infrared Hyperspectral Imager. SIMBIOSYS will characterize the hermean surface in terms of surface morphology, volcanism, global tectonics, and chemical composition. The aim of this work is to describe a tool for the radiometric response prediction of the three SIMBIOSYS channels. Given the spectral properties of the surface, the instrument characteristics, and the geometrical conditions of the observation, the realized SIMBIOSYS simulator is capable of estimating the expected signal and integration times for the entire mission lifetime. In the simulator the spectral radiance entering the instrument optical apertures has been modelled using a Hapke reflectance model implementing the parameters expected for the hermean surface. The instrument performances are simulated by means of calibrated optical and detectors responses. The simulator employs the SPICE (Spacecraft, Planet, Instrument, C-matrix, Environment) toolkit software, which allows us to know for each epoch the exact position of the MPO with respect to the planet surface and the Sun.

Key words: methods: numerical – techniques: high angular resolution – techniques: image processing – techniques: imaging spectroscopy – planets and satellites: surfaces.

1 INTRODUCTION

Given the low number of space mission that visited Mercury (Blewett et al. 2009), many open questions concerning the geological evolution of the planet, the anomalous ratio between metal and silicate, the magnetic field generation and the evolution of exosphere remain to be addressed (Benkhoff et al. 2010; Cremonese et al., in preparation). The investigation of surface characteristics is crucial to study the geological history of Mercury, which includes the crustal differentiation and resurfacing, the volcanism, the tectonics, and the surface–atmosphere interaction. To investigate these topics, high-resolution data are required. The first images acquired by Mariner 10 cover 45 per cent of the entire hermean surface at the average resolution of about 1 km px^{-1} and few images at about 100 m px^{-1} (Murray 1975; Flamini et al. 2010). A more extended coverage of the hermean surface has been achieved by the Mercury Dual Imaging System (MDIS), on board NASA MESSENGER spacecraft, which provided higher resolution images of the hermean surface features (Hawkins et al. 2007). The next challenging mission towards Mercury is the ESA cornerstone mission BepiColombo, launched on 2018 October 20, which will reach Mercury in 2025, improving the planet characterization.

★ E-mail: alessandra.slemer@pd.ifn.cnr.it

BepiColombo is an interdisciplinary mission through a partnership between the European Space Agency (ESA) and the Japan Aerospace Exploration Agency (JAXA) (Schulz & Benkhoff 2006). The BepiColombo spacecraft includes two modules: the Mercury Planetary Orbiter (MPO) and the Mercury Magnetospheric Orbiter (MMO), which will study the planet and its environment.

Spectrometer and Imagers for MPO BepiColombo Integrated Observatory SYStem (SIMBIOSYS) is one of the 11 instruments on-board of the MPO. It will give a crucial contribution to the analysis of geological and mineralogical features that characterize the hermean surface.

The SIMBIOSYS instrument includes three channels: a High Resolution Imaging Channel (HRIC), an imaging system with stereo capabilities, which is the Stereoscopic imaging Channel (STC) and a hyperspectral imager in the visible and near-IR range, named Visible and near Infrared Hyperspectral Imager (VIHI). HRIC is a camera for high-resolution imaging (6–12 m px^{-1}) in panchromatic and broad-band filters; STC will perform 60–120 m px^{-1} of spatial resolution global mapping in stereo mode and colour imaging in selected areas, and VIHI will perform imaging spectroscopy in the 400–2000 nm spectral range with a max spatial resolution of 100 m px^{-1}. A highly integrated configuration is adopted to maximize the scientific return and minimize the resource requirements, primarily mass and power.

The main scientific goals of SIMBIOSYS are: (i) to map the whole hermean surface in the visible and near-IR, (ii) to give the 3D surface reconstruction, (iii) to image selected regions at high spatial resolution in order to investigate the morphology and chemical composition of surface features. To fulfill these goals, it is necessary to predict the channels performance and to plan the observation strategy during the different phases of the mission. For these purposes, an instrument simulator has been developed.

To calculate the expected signal detected by each SIMBIOSYS channel, the simulator takes into account: the SPICE (Spacecraft, Planet, Instrument, C-matrix, Environment) toolkit software (Acton et al. 2005) to simulate the orbital configuration during the entire mission, the Hapke reflectance model to derive the hermean expected radiance (Hapke 2012; Hapke et al. 2012), and the instrument optical response. For each point along the orbit during the mission lifetime, the simulator produces a series of outputs that can be divided into three groups:

(i) the output values related to the geometrical properties of the spacecraft and the SIMBIOSYS channels;
(ii) the radiometric outputs that include the reflectance of the planet, the incoming radiance, and the signal expected on the detector;
(iii) the output values that measure the performance of each SIMBIOSYS channel.

Each group will be described in detail in Section 4.

The paper is structured as follows. First, the BepiColombo mission profile (Section 2) and the SIMBIOSYS channels characteristics (Section 3) will be introduced. Then, Sections 4 and 5 will describe the SIMBIOSYS simulator and the radiometric model. Finally, Section 6 is devoted to the application of the simulator to each SIMBIOSYS channel.

2 BEPICOLOMBO MISSION PROFILE, MERCURY, AND MPO ORBITAL DATA

The BepiColombo Mercury Composite Spacecraft has been launched on 2018 October 20 on an Ariane 5 from Kourou.

Table 1. Some Mercury orbit parameters.

	Perihelion	Aphelion
Mercury-Sun dist. (km)	4.6×10^7	6.892×10^7
Mercury vel (km s^{-1})	58.98	38.86
Mercury rotation period (h)	1407.6	1407.6

The spacecraft will take 7 yr to reach the planet Mercury. Nine flybys are needed to redirect the Mercury Composite Spacecraft towards Mercury: one of Earth, two of Venus, and six around Mercury to decelerate the spacecraft and stabilize it on the nominal orbit.

For the interplanetary cruise the solar-electric propulsion will be used, while chemical propulsion engines will allow MPO to get captured and inserted in the Mercury orbit, starting the operational phase in 2026 March. The nominal mission is expected to last 1 yr, with the possibility of another 1 yr of extended mission.

The Mercury orbit is elliptic and characterized by low eccentricity (0.205632) and short semimajor axis (0.387098 AU). The Mercury velocity and distance with respect to the Sun vary during the revolution. The details on the Mercury orbit around the Sun are reported in Table 1.

The HRIC and VIHI channels could observe all over the hermean year, i.e. for all the true anomaly (ν) values, while STC planned observations are foreseen only in the true anomaly interval $90^\circ - 270^\circ$, which includes both the calibration phases (for true anomaly $90^\circ \leq \nu < 138^\circ$ and $222^\circ < \nu \leq 270^\circ$) and the scientific acquisitions (for true anomaly in the interval $138^\circ - 222^\circ$).

Fig. 1 shows a schematic representation of the Mercury orbit around the Sun where the arc in bold refers to the part of the orbit during which STC will be operative.

The three axis stabilized MPO spacecraft orbits around Mercury on a polar and elliptic orbit. At the beginning of the science mission (first orbit), its eccentricity is 0.1486, the semimajor axis is 3430 km, the altitudes at periherm and apoherm are respectively 480 and 1500 km.

During the mission, the argument of the periherm decreases, from 16° at the beginning of the mission to -45° at the end of the extended mission. Also the minimum altitude of the spacecraft with respect to the planet surface changes, from 480 km at the beginning to 250 km at the end of the mission (Jehn 2015).

3 THE SIMBIOSYS INSTRUMENT

SIMBIOSYS is composed by three different channels sharing a common Main Electronics and power supply. Each channel has its own optical head, detector, thermal hardware, proximity electronics and electrical interface for power supply, data, and telemetry links (Flamini et al. 2010). The measurement strategy is based on the coordinated operations of the three channels forming SIMBIOSYS. In this section, we briefly describe the main characteristics of each channel.

3.1 The STC channel

STC is a double wide angle camera designed to image specific portions of the hermean surface from two different perspectives with the push-frame acquisition technique, providing panchromatic (PAN) stereo image pairs necessary for the global Digital Terrain Model reconstruction (Flamini et al. 2010). The design of the camera consists of two sub-channels which acquire the sun-light refracted

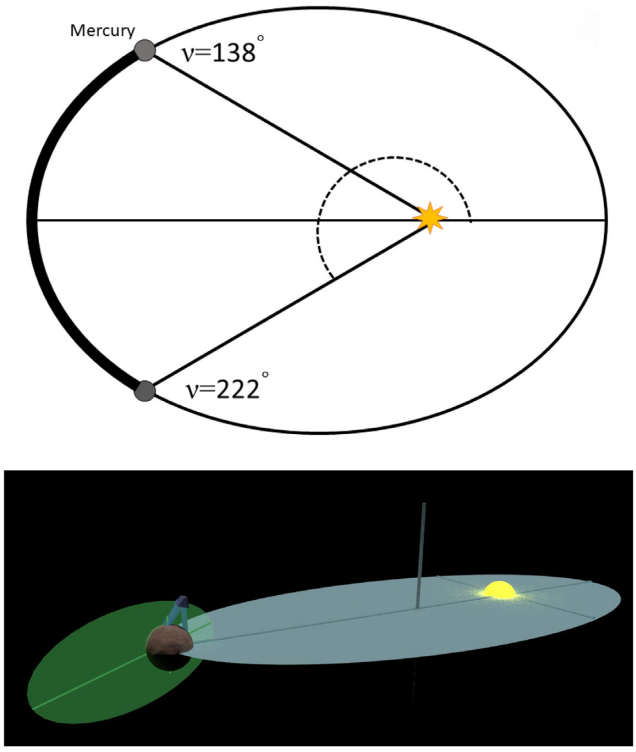

Figure 1. Top panel: A simplified 2D scheme of the hermean orbit around the Sun. The arc in bold style shows the part of the orbit where STC will acquire data. Bottom panel: a 3D Scheme of the plane of the hermean orbit around sun (light blue) and the plane of the MPO orbit around Mercury (green). The objects are not in real scale.

by hermean surface and focus it on one common detector. Each sub-channel line of sight forms an angle of 20° and −20° with respect to the nadir direction. The optical characteristics of STC and the scientific requirements are shown in Table 2 (Da Deppo et al. 2016).

For each sub-channel, STC can acquire simultaneously three quasi-contiguous areas of the hermean surface in different colours in order to investigate its mineralogical composition (Slemer et al. 2018). The nominal Field of View (FoV) of each sub-channel is 5.38° × 4.8°, including gaps, while the scientific dimension of the FoV is 5.38° × 3.2°. The latter FoV is divided in three portions that correspond to each filter of the sub-channel considered (5.38° × 2.31° for panchromatic filter, and 5.38° × 0.38° for colour filters). A schematic representation of the FoV of the filters of STC has been shown is Fig. 2.

The STC detector is a 2048 × 2048 hybrid Si-PIN based on CMOS technology, which combines low read-out-noise, compactness, low parasitic light, capability of image acquisition with short ms-exposure times (Simioni et al. 2017). It is back illuminated with pixel size of 10 µm (Mills, Drab & Gin 2009). A detector based on CMOS technology has been chosen instead of a CCD thanks to rad-hard characteristics and the possibility to acquire different detector windows at the same time.

The detector acquisition strategy is the so-called 'integrate then read' mode, which allows us to avoid a mechanical shutter (Simioni et al. 2017; Slemer et al. 2019b). Furthermore, the CMOS detector allows us to reach millisecond exposure times needed to avoid the image smearing due to the motion of the spacecraft with respect to hermean surface (Slemer et al. 2019a).

3.2 The HRIC channel

The main feature of SIMBIOSYS HRIC is a spatial resolution of 6 m px^{-1} at 480 km from the planet surface. The HRIC's primary task is to provide high-resolution images of selected hermean surface features (Zusi et al. 2019).

The HRIC optical design is based on a catadioptric Ritchey–Chretien telescope with a focal length of 800 mm, modified with a dedicated refractive field corrector. This configuration gives resolution of 2.6 arcmin for a pixel size of 10 µm. The focal ratio of the instrument is f/8.9. The optical design has been conceived to be diffraction limited at 400 nm (Zusi et al. 2019).

HRIC detector is of the same type adopted for STC. The use of a 2kx2k detector guarantees a coverage of a squared FoV of 1.47°.

To investigate the geo-mineralogical properties of the hermean surface, four filters are deposited over the detector window: a panchromatic filter (with central wavelength of 650 nm and bandwidth 500 nm), and three broad-band filters (with central wavelength of 550, 750, and 880 nm respectively and bandwidth of 40 nm), as shown in Fig. 3.

3.3 The VIHI channel

The third SIMBIOSYS channel is the VIHI, which has been realized to investigate the hermean surface composition. The VIHI channel has been conceived as a Schmidt telescope coupled with a diffraction grating Littrow spectrometer, which has been designed by Leonardo S.p.A. The spectrometer operates in the wavelength range from 0.4 to 2.0 µm. The optical design includes also two dioptric doublets that correct the aberrations both in the telescope and in the spectrograph optical path (Capaccioni et al. 2010).

The diffraction grating disperses the image of the slit on a 2D 256 × 256 pixel HgCdTe disperses the image of the slit. The instrument is equipped with an electromechanical shutter to measure the internal background and dark current. The pixel pitch of VIHI detector is 40 × 40 µm and the full-well capacity is 2 Me$^-$. The nominal detector operative temperature value is 220 K.

The image acquisition is through a pushbroom mode (Altieri et al. 2017). The field of view (FoV) width is 3.7°, with 256 spatial pixels each having a 250 µrad of instantaneous FoV (IFoV) (Capaccioni et al. 2010). The main optical parameters of VIHI are summarized in Table 4.

4 SIMBIOSYS SIMULATOR

The aim of the SIMBIOSYS simulator is to predict the instrument performance to assist in the definition of the observation strategy all over the mission. The pipeline of this simulator is represented in Fig. 4.

The simulator, computed with the Interactive Data Language (IDL, provided by Harris), receives in input the time of the simulation and the name of the SIMBIOSYS channel to be considered. The simulator uses the SPICE toolkit software (Acton et al. 2005) with the kernels of BepiColombo mission to derive the geometrical information needed to retrieve the output data.

The outputs of the SIMBIOSYS simulator can be divided in three groups:

(i) the geometrical values related to the spacecraft and the channels, which include both the general information about the spacecraft (altitude with respect to the ground, velocity, etc.) and the information for each filter (FoV, footprints, and their position

Table 2. Optical characteristics and scientific requirements of STC. Scientific requirements are defined considering panchromatic filter at periherm of the first orbit (480 km) (Slemer et al. 2018).

Optical characteristics	Scientific requirements (Global Mapping)
Optical concept	Catadioptric: off-axis portion of a modified Schmidt telescope with folding mirror fore-optics
Stereo solution	Two optical channels tilted of ±20° with respect to the nadir direction, with a common detector and most of the optical elements
Effective focal length	95.2 mm
Entrance pupil	15 mm (diameter)
f/number	6.3
IFoV (Instantaneous Field of View)	105 μrad
Distortion	< 0.3 percent Simioni et al. (2019)
FoV (cross track)	5.38°
FoV (along track)	2.4° for panchromatic and 0.38° for colour filters
Fraction of diffraction ensquared energy (EE)	> 70 percent inside 1 pixel
Diffraction modulation transfer function (MTF)	> 60 percent at Nyquist Frequency
Wavelength coverage	410–930 nm (6 filters)
Filters	PAN (700 ± 100 nm) 2 filters one for each sub-channel
	F420 (420 ± 10 nm) (sub-channel H)
	F550 (550 ± 10 nm) (sub-channel L)
	F750 (750 ± 10 nm) (sub-channel H)
	F920 (920 ± 10 nm) (sub-channel L)
Parameter	**Scientific requirements (Global Mapping)**
Scale factor (along-track x cross track)	61.2 × 55.1 m px^{-1}
Swath (along track x cross track)	23.5 × 4.9 km
Stereoscopic properties	±21.375° bore-sight angle versus nadir
Vertical accuracy	80 m

Table 3. HRIC optical parameters (Zusi et al. 2019).

Parameters	Values
Entrance pupil	90 mm (diameter)
Effective focal length	800 mm
f/number	8.9
central obscuration	10 percent diameter
FoV	1.47°
IFoV	12.5 μrad
Scale	6 m px^{-1} from 480 km
Wavelength coverage	400–900 nm
Filters	PAN (650 ± 250 nm)
	F550 (550 ± 20 nm)
	F750 (750 ± 20 nm)
	F880 (880 ± 20 nm)

in latitude and longitude, on-ground pixel dimension, boresight velocity);

(ii) the radiometric outputs, which include the reflectance of the planet, the radiance, and the expected signal measured by the detector;

(iii) the quantities related to the channel performance, such as the integration time, whose definition is needed to avoid the detector saturation, the expected dark current, and the smearing time. The value considered for SIMBIOSYS smearing is equivalent to the time in which the observed scene moves of 1/4 px.

The output values can be obtained for the entire mission in form of table, xmls files, or output graph. In this work, different reference values of true anomaly have been considered: the values $\nu = 140°$, 180°, and 220° for STC, and $\nu = 140°$, 180°, and 0° for VIHI and HRIC. The output values on one entire orbit of MPO around Mercury will be then presented.

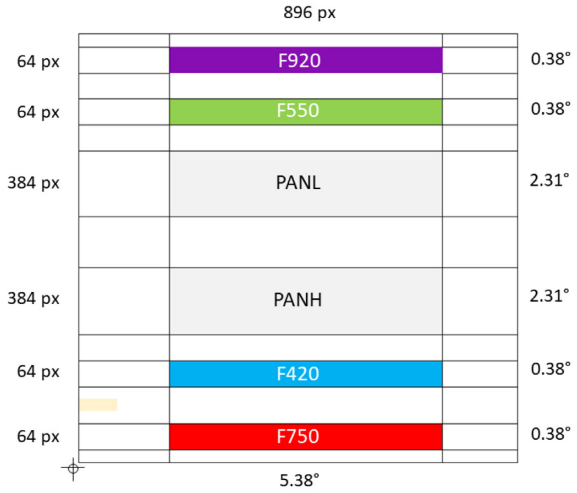

Figure 2. Schematic representation of the FoV of the filters of STC channel and their position on the CMOS detector.

While the first category of outputs has been obtained only with the SPICE kernel based reduction, the last two groups of output values have been calculated by developing a radiometric model. The radiometric model developed in this work is described in the following section.

5 SIMBIOSYS RADIOMETRIC MODEL

The radiometric model gives a mathematical description of the radiance-signal conversion process. In order to determine the radiance incoming to the instrument, the radiance of the surface has to be estimated knowing the illumination condition and the viewing geometry (observational parameters). A reflectance model

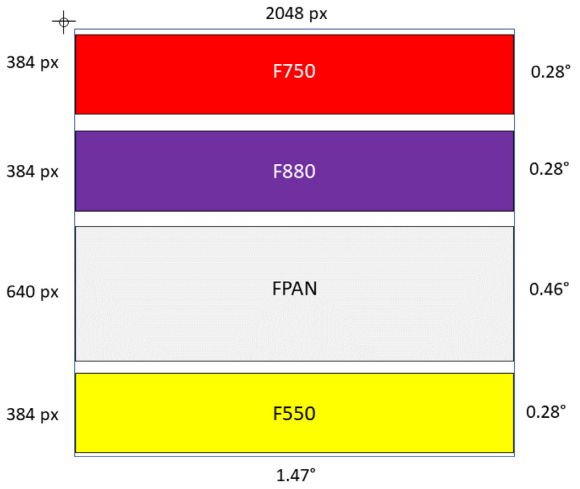

Figure 3. Schematic representation of the FoV of the filters of HRIC channel and their position on the CMOS detector.

Table 4. VIHI optical parameters (Capaccioni et al. 2010).

Parameters	Values
Entrance pupil	25 mm (diameter)
Effective focal length	160 mm
f/number	6.4
FoV	64.0 × 0.25 mrad
IFoV	0.25x0.25 mrad
Scale	120 m px^{-1} from 480 km
Wavelength coverage	0.4–2.0 μm
Spatial samples	256
Spectral bands	256
Spectral dispersion	6.25 nm per band

estimates the fraction of light reflected by a surface depending on its morphological, compositional, and geometrical properties. Knowing the radiance that arrives at the entrance pupil of the instrument, it is possible to convert this quantity to the signal measured by the instrument. The radiance-to-signal conversion depends on both the optical system of the instrument and the detector behaviour. In particular, it is necessary to know the lens and mirrors transmittance, the filter efficiencies, the quantum efficiency, and the amount of noise that affects the detector.

This section describes which elements are involved in the radiometric model definition. For the SIMBIOSYS instrument the Hapke reflectance model has been used (Hapke 2002; Hapke 2012; Hapke et al. 2012), coupled with the parameters derived by Domingue et al. (2016).

5.1 Surface viewing geometry and illumination parameters

The spectral radiance reaching the detector is first depending on how the light is reflected by the hermean surface. The amount of the reflected light is determined by the incidence (i), emission (e), and phase (α) angles. The incidence angle is the one between the direction of the Sun light hitting the observed surface and the surface normal. The emission angle is defined by the surface normal and the light ray that is detected by the instrument, while the phase angle is the angle between the incoming Sun radiation and the direction of observation. In general the incident, emission and phase angles sit in three different planes. Therefore, the phase angle is always

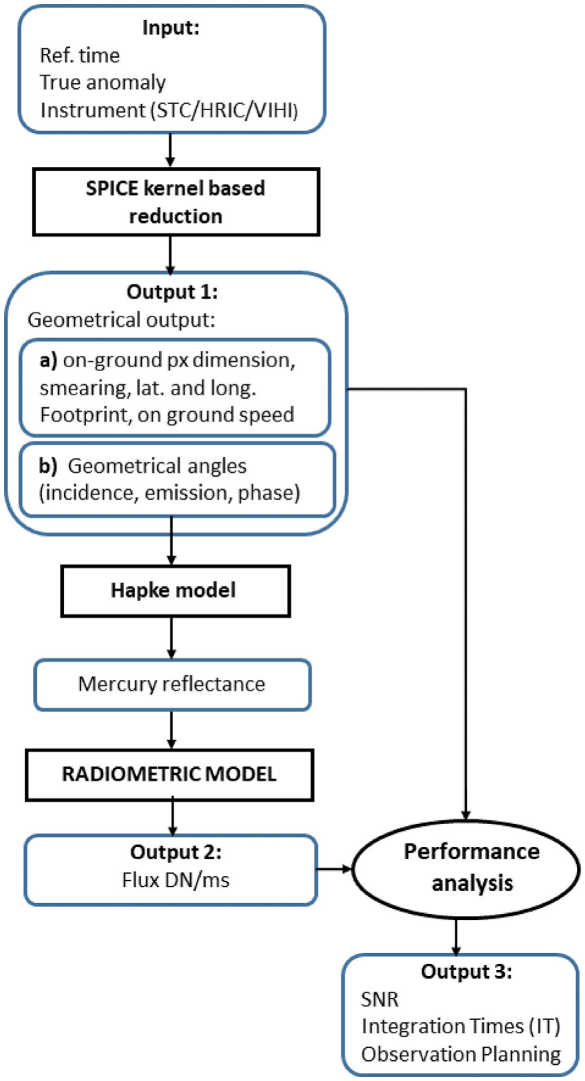

Figure 4. Flowchart of the SIMBIOSYS simulator. The blue squares represent the input and output of the model, while the dark squares show the model used in the simulator.

lower – equal to the sum of i and e. The angles i, e, and α depend on both the position of MPO with respect to the planet and the position of Mercury in its orbit around the Sun. Thus, the light detected is a function of the relative positions of MPO, Mercury, and the Sun. In Fig. 5 it is reported as a sketch of the periherm part of the MPO orbit around Mercury. As an example, the geometrical viewing and illumination conditions of a typical STC observation are highlighted.

5.2 Radiance of Mercury surface

In order to determine the hermean radiance, we have to consider the fraction of Sun light that impacts on the planet surface.

The spectral radiance B(λ)[W/(m^{2}msr)] of the Sun is assumed as the Black Body (BB) distribution described by the Planck's law:

$$B(\lambda) = \frac{hc^2}{\lambda^5} \frac{1}{e^{hc/\lambda k_B T_{eff}} - 1}, \quad (1)$$

where h is the Planck constant, c the speed of light in vacuum, λ the wavelength in meters, k_B the Boltzmann constant (Slemer et al.

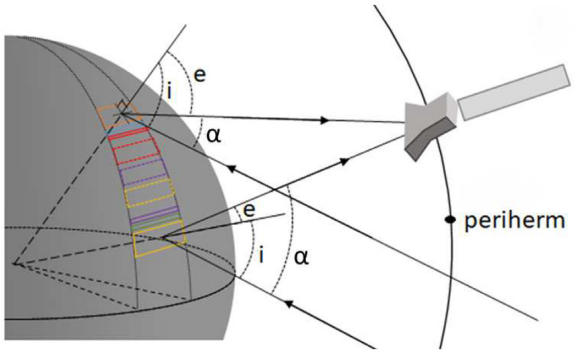

Figure 5. A 3D schematic representation of the periherm part of the MPO orbit around Mercury. In particular, the surface viewing geometrical conditions of the two sub-channels of STC are highlighted.

2018). The term $T_{eff} = 5776$ K is the effective temperature of the Sun. The solar irradiance $I_{\odot}(\lambda)$[W/(m^{2}m)] at a given distance (r) from the Sun is defined by:

$$I_{\odot}(\lambda) = B(\lambda) \cdot \pi \left(\frac{R_{\odot}}{r} \right)^2, \tag{2}$$

where $R_{\odot}$ is the solar radius. The term $\pi(R_{\odot}/r)^2$ is the solid angle that determines the radiance incoming to each hermean surface element, for each wavelength. The Sun–Mercury distance is a function of the true anomaly:

$$r(\nu) = \frac{a(1-e^2)}{1 + e \cdot \cos(\nu)}, \tag{3}$$

where e is the orbit eccentricity, ν the true anomaly, and a the semimajor axis. The Mercury radiance can be calculated as follows:

$$I(\lambda, \nu) = I_{\odot}(\lambda, \nu) R(i, e, \alpha), \tag{4}$$

where R(i, e, α) represents the reflectance function, which depends on the incident (i), emission (e), and phase (α) angles formed by the (light) rays with the surface point observed (Slemer et al. 2018).

5.2.1 *Reflectance model*

The Hapke reflectance model describes and accounts for reflective properties of the hermean surface (including the radiative transfer equations). The surface roughness and porosity, grain scattering properties, and the opposition surge are considered in the model. The opposition surge is the steep increase in reflectance at small phase angles, which is due to two different mechanisms: the Shadow-Hiding Opposition Effect (SHOE), and the Coherent Back-scatter Opposition Effect (CBOE) (Domingue et al. 2016).

The reflectance derived from the Hapke model is a function of the observational parameters, i.e incidence, emission, and phase angles, and it is expressed by the following equation:

$$R(i, e, \alpha)_{\lambda} = K \frac{w}{4\pi} \frac{\mu_{0e}}{\mu_e + \mu_{0e}} \left[p(\alpha)[1 + B_{S0} B_S(\alpha)] + \left[H\left(\frac{\mu_{0e}}{K}\right) H\left(\frac{\mu_e}{K}\right) - 1 \right] \right] \times [1 + B_{C0} B_C(\alpha)] \sigma(i, e, \alpha, \theta), \tag{5}$$

where μ_{0e} and μ_e are, respectively, the cosines of the incidence and emission angles modified to include surface roughness. μ_{0e} and μ_e depend by the incident, emission, and phase angles and by the roughness of the surface. K is the porosity term, which depends on the filling factor Φ (the amount of regolith volume filled by a material). The term w is the volume-averaged single scattering albedo, and p(α) stands for the Henyey–Greenstein function. $B_S(\alpha)$ defines the SHOE effect, with amplitude B_{S0}. The expression $B_C(\alpha)$ and the parameter B_{C0} specify the CBOE effect. The H-function is an algebraic expression that depends only on both μ_{0e} and the porosity K. Finally, the large-scale roughness $\sigma(i, e, \alpha, \theta)$, depends on the scattering angles and on the surface roughness expression θ (Domingue et al. 2015, 2016). A more detailed description of all these quantities has been given in the appendix section (A).

Since the equation (5) depends on the wavelength of the incident light, the Hapke's model parameters have been estimated for different values of λ. The most recent estimations of Hapke's spectral parameters are obtained by Hapke et al. (2012) and Domingue et al. (2015, 2016) using the high-resolution images provided by the MESSENGER spacecraft prior to 2011 May 24 (Domingue et al. 2015). The parameters are derived for each MDIS filter. The present analysis takes into account the Matabei data set analysed in the study of Domingue et al. (2015). In this work we consider the Matabei data set derived by Domingue et al. (2015), which includes the single scattering albedo, the single-particle scattering, and the surface roughness parameters.

The coherent backscatter opposition parameters are set to the values $b_c = 2.3$ and $b_c = 0.075$, while the shadow hiding opposition parameter (b_s) is set equal to zero. For further details see Domingue et al. (2015, 2016).

A quadratic interpolation has been used to obtain the vales of the parameters for all the wavelength between 300 and 1100 nm. The result consists in a series of functions, one for each parameter, which will be included in the equation (5). The output is a reflectance function for the 300–1100 nm wavelength interval, which depends on the illumination angles (i, e, α) and on the hermean area observed.

The reflectance has been obtained for each SIMBIOSYS channel. The most interesting results are those obtained for STC, which has a non-nadiral configuration and thus the reflectance depends on the sub-channel considered.

Fig. 6 shows the reflectance obtained with the Hapke model for HRIC and for both the sub-channels of STC (left-hand panel sub-channel L, CH-L, and right-hand panel sub-channel H, CH-H), and for two different positions of the spacecraft with respect to Mercury.

The blue dashed line corresponds to the reflectance calculated when the spacecraft is above the zero latitude, while the red solid line indicates the reflectance obtained when the spacecraft is at periherm. The two spacecraft configurations result in different reflectance curves for each channel case. Indeed the latitude of periherm is 16° and, hence, the combination of incidence, emission, and phase angles changes depending on the spacecraft position. The two spacecraft configuration result in different reflectance curves for each channel case. Indeed the argument of periherm is 16° and, hence, the combination of incidence, emission, and phase angles changes depending on the spacecraft position. Furthermore, the reflectance seen from sub-channel L and sub-channel H when the spacecraft is over the zero-latitude are not exactly equal. This fact is a consequence of the spacecraft position sampling calculated by the simulator, because the latitude of the sub-nadiral point of the spacecraft is not exactly zero (0.4031°) and so the values of the sub-channel L and sub-channel H radiance are not exactly equal.

Fig. 7 shows the hermean expected radiance for both sub-channels of STC (sub-channel L in the top panel and sub-channel H in the bottom one), calculated assuming the Sun as a Black Body with the effective temperature of 5776 K. The back-reflected spectral

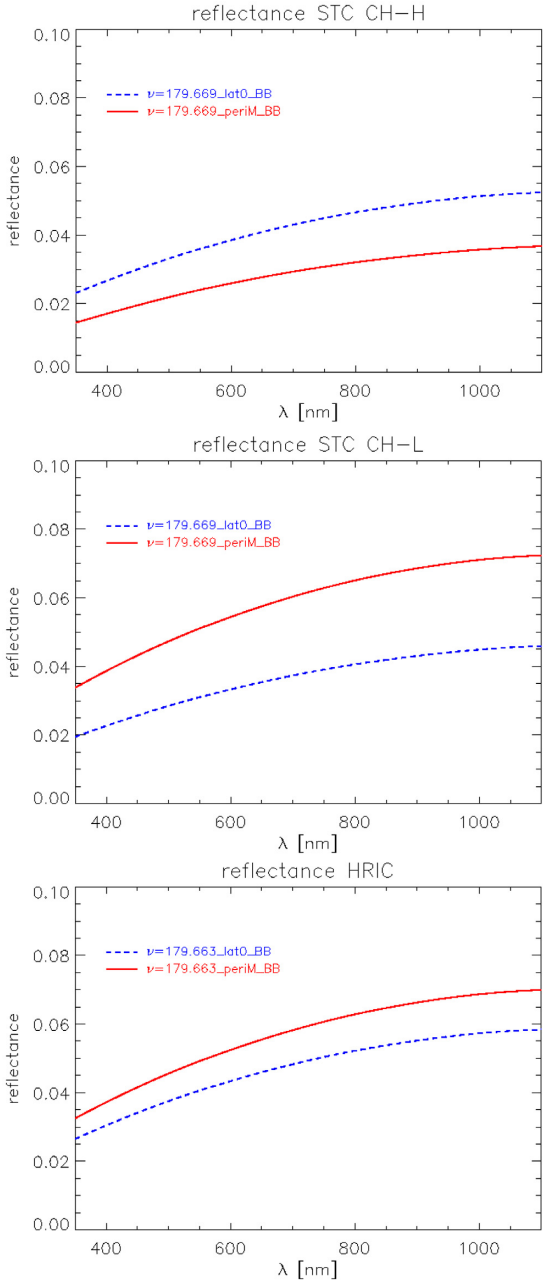

Figure 6. The reflectance curves for both the STC sub-channel H and L (top and middle panel), and for the HRIC channel (bottom panel). The blue dashed line and the red solid line correspond to the reflectance values for (i) Mercury in aphelion and spacecraft above the latitude 0° and (ii) the spacecraft at periherm, respectively.

radiance from the hermean surface has been calculated at aphelion and for two specific positions along the orbit (blue dashed line for periherm and red solid line for the point in which the spacecraft is above the latitude 0 of Mercury). The green dash-dotted line shows the previous expected radiance, which has been calculated considering a nadiral viewing condition for a periherm at 0 latitude, constant albedo (0.12), and assuming the hermean surface to be a perfect Lambertian diffuser (Da Deppo et al. 2016). The comparison between the two methods shows that the hermean radiance seen by the two STC sub-channels varies significantly when the actual

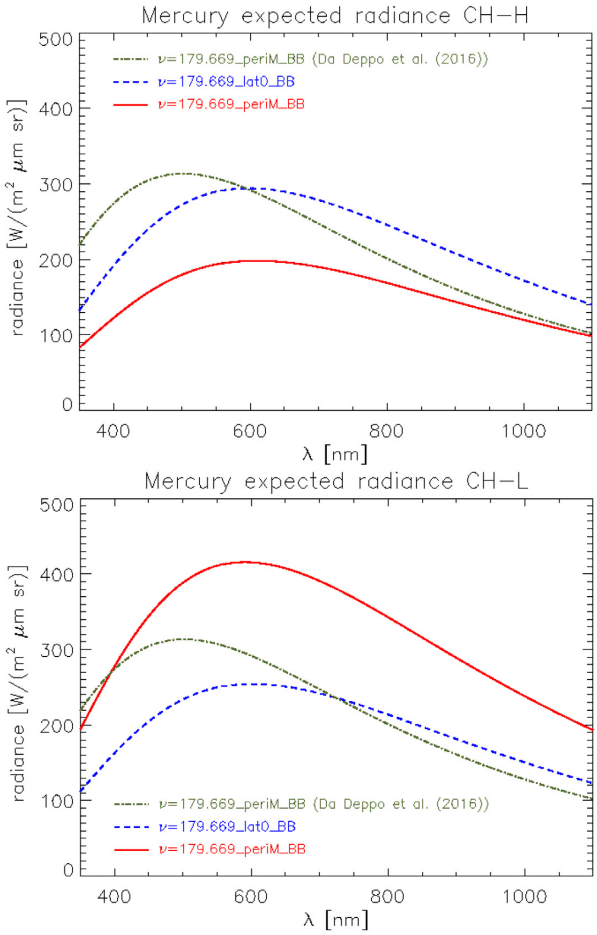

Figure 7. Mercury expected radiance for sub-channel H (top panel), and sub-channel L (bottom panel) of STC. Different colours and line styles stand for different position of the spacecraft w.r.t. to Mercury (red solid line refers to the spacecraft at periherm and blue dashed line for the spacecraft at latitude zero). The green dash-dotted line is the radiance obtained by Da Deppo et al. (2016) for Mercury at aphelion and the spacecraft at periherm.

observing conditions and the Hapke reflectance model are taken into account.

6 THE RADIOMETRIC MODEL

The calculation of the radiance coming from the source is necessary to estimate the value measured by the detector. In the following sections the radiance and the signal will be estimated varying the true anomaly of Mercury and the position of the spacecraft around the planet.

The estimation of the source radiance includes the contributions both of hermean thermal radiation and the Sun Black body radiation reflected by the planet surface. Since the maximum of the thermal radiation is at 10 μm it can be considered negligible because it is out of the SIMBIOSYS spectral range, which spans from 400 to 930 nm for STC and HRIC, and from 400 to 2000 nm for VIHI (Slemer et al. 2018).

The spectral radiant signal rate $\phi(\lambda)[\mathrm{W\,nm^{-1}}]$, which arrives at the entrance pupil of each channel, can be expressed as:

$$\phi(\lambda) = I(\lambda, \nu) \cdot A \tag{6}$$

in which the quantity I(λ) represents the spectral irradiance coming from the hermean surface and $A = \pi(D/2)^2$ is the area of the entrance pupil with diameter D. The spectral irradiance is obtained by multiplying the source spectral radiance L(λ) with the solid angle subtended by the observed area of the planet surface. Usually the solid angle considered is that subtended by one pixel $\Omega_{px} = IFoV^2$ (Da Deppo et al. 2016).

The signal rate that hits the detector is lower than the one at the entrance pupil because the optics (T(λ)) and filter (F(λ)) transmissions properties have to be considered:

$$\phi_{det}(\lambda) = \phi(\lambda) \cdot T(\lambda) \cdot F(\lambda). \quad (7)$$

The quantity $\phi_{det}(\lambda)$ is measured in [W nm^{-1}].

The detector measures the signal in Digital Number (DN), so that the signal rate $\phi_{det}(\lambda)$ has to be divided by the energy of the photons and it has to be multiplied by the quantum efficiency of the detector (QE(λ)). This result (with measurement unit [e$^-$/(nm · ms)]) has to be divided by the Inverse Gain (IG), which represents the number of electrons that correspond to 1 DN. The results is the signal rate and it is measured in DN ms^{-1}:

$$\phi_e(\lambda) = \frac{1}{IG} \cdot \phi_{det}(\lambda) \cdot \left(\frac{\lambda}{hc}\right) \cdot QE(\lambda). \quad (8)$$

The detectors of STC and HRIC have the IG equal to 7e$^-$/DN (Da Deppo et al. 2016), while the VIHI IG is ∼150e$^-$/DN.

In order to obtain the signal rate for a specific filter, equation (8) has to be integrated in the wavelength interval that corresponds to the band-width of the filter considered:

$$F_e = \frac{1}{IG} \cdot \int_{\Delta\lambda} \phi_e(\lambda) \cdot d\lambda, \quad (9)$$

where Δλ is the bandwidth of the filter considered.

Combining the equations (6), (7), and (8) the following complete expression has been obtained:

$$F = \frac{F_e}{IG} = \frac{A}{IG \cdot hc} \int_{\Delta\lambda} I(\lambda) \cdot T(\lambda) \cdot F(\lambda) \cdot QE(\lambda) \cdot \lambda \cdot d\lambda$$
$$= \frac{1}{IG} \int_{\Delta\lambda} I(\lambda) \cdot ITF(\lambda) \cdot \lambda \cdot d\lambda. \quad (10)$$

The ITF expression stands for the instrument transfer function, which includes the transmission functions of the optical components and the QE of the detector.

The equation (10) permits us to calculate the signal rate measured by the detector by knowing the incoming radiance, which depends on the illumination angles (i, e, α) and thus is related to the position of the spacecraft in the hermean frame. The following section shows the signal rates estimated for the three channels of SIMBIOSYS for the most representative scenarios of the BepiColombo mission.

7 OUTPUTS OF THE SIMBIOSYS SIMULATOR

As explained in Section 4, the information taken from SPICE kernel allows us to derive some useful quantities related to the orbit of the Mercury Planetary Orbiter during the mission. The Fig. 8 shows an example of quantities that describe the spacecraft status for one specific orbit around Mercury (which is 2 h and 20 min). The top panel shows the spacecraft altitude, while the bottom panel represents the velocity of the spacecraft and its ground projection. The x-axis represents the relative time with respect to the absolute time corresponding to the periherm. These values have been calculated at the beginning of the mission.

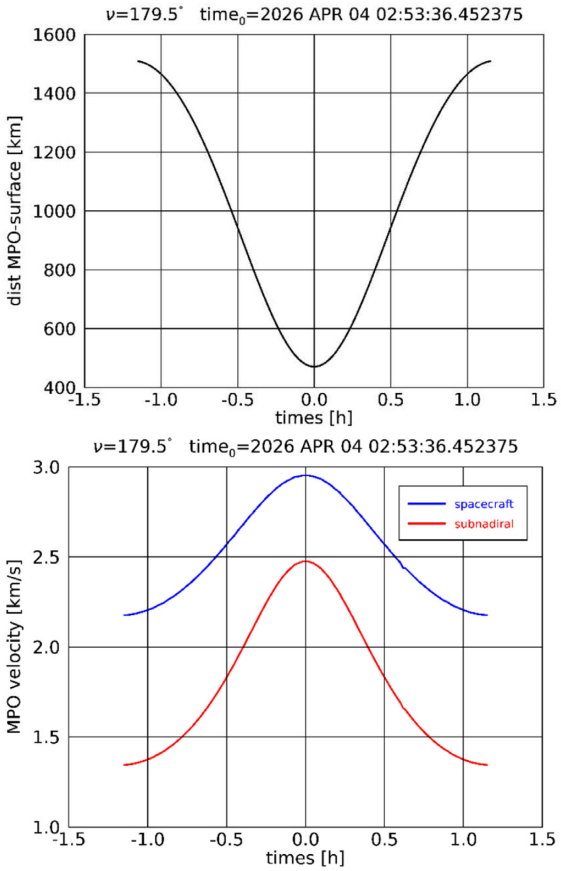

Figure 8. Altitude of the spacecraft with respect to the ground level (top panel), and velocity of the spacecraft and its subnadiral correspondent point (bottom panel).

Since the spacecraft altitude at periherm position changes during the mission (from 480 km to less than 300 km), it is possible to predict the evolution of the altitude of periherm during the entire mission, and thus is possible to derive a great number of useful quantities (e.g. spatial resolution, dimension of footprints, time interval between two subsequent acquisitions).

Fig. 8 shows also that the minimum of the spacecraft altitude curve is reached at periherm (zero value of x-axis), which does not coincide with the latitude zero.

This section shows some of the outputs obtained through the application of the simulator of the SIMBIOSYS channels, which can be useful for the instrument performance analysis and for the observation strategy.

7.1 Expected signal and integration time

The expected signal rate, expressed in equation (10), depends on the hermean radiance and on the optical and detector characteristics of the SIMBIOSYS channel considered. In this section we show the main outputs derived by applying the simulator to the three channels of SIMBIOSYS.

7.1.1 STC outputs

The results obtained for the STC take into account the transmission values of all filters (F(λ)) and the detector QE (QE(λ)) reported in Da Deppo et al. (2016). The value of the optical components

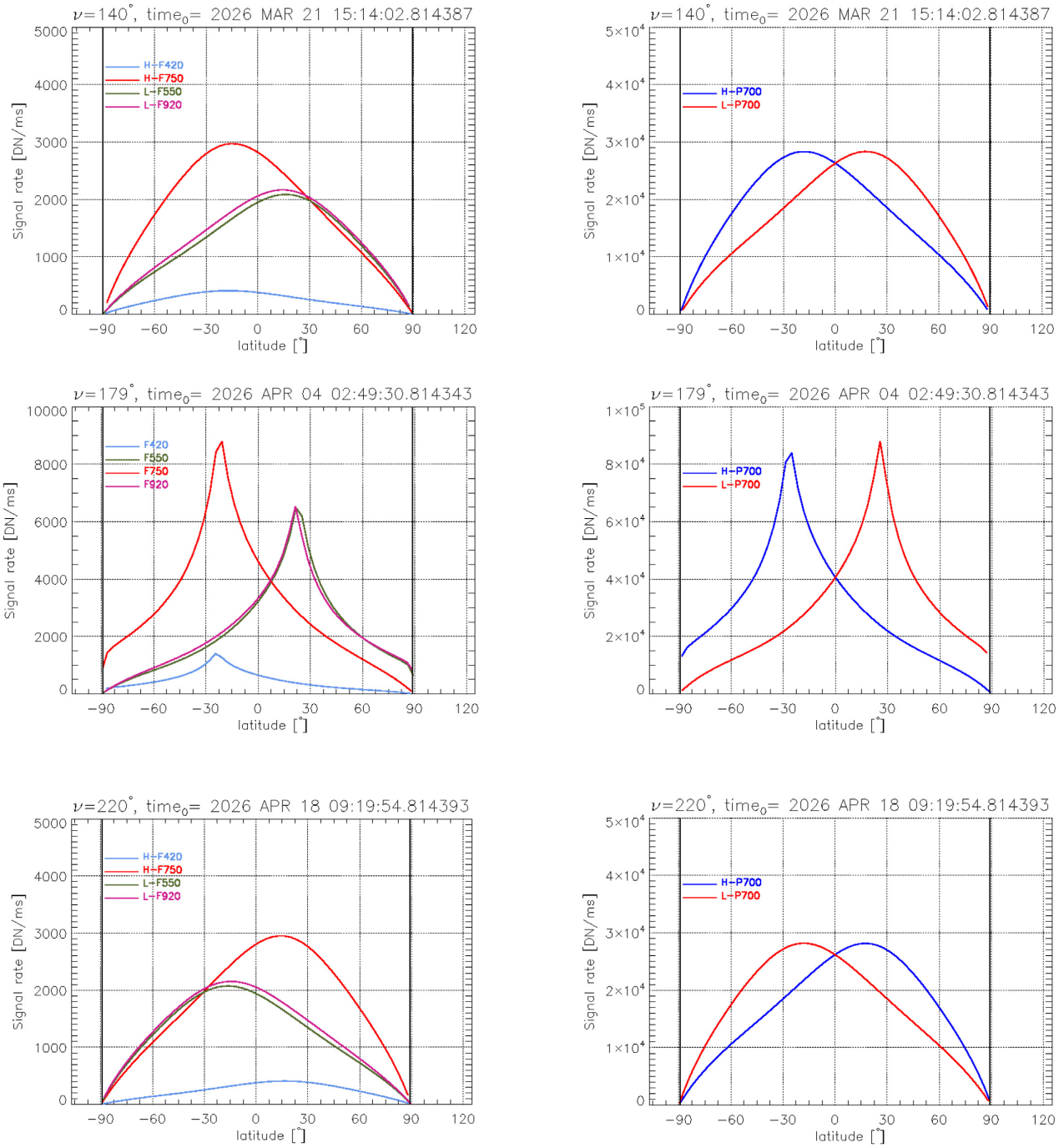

Figure 9. Expected signal rate in DN ms^{-1} for STC. The signal rate, in function of the boresight latitude, is shown for colour and panchromatic filters (left-hand side and right-hand side, respectively). The results are obtained for different values of true anomaly. The variable $time_0$ is the absolute time correspondent to the spacecraft passage over the zero latitude. The dark current obtained in Leonardo S.p.A at nominal temperature T = 268K and repetition time of 2 s has been taken into account to derive the results. From top to bottom, the three panels refer to three different true anomaly values ($\nu = 140°, 179°, 220°$).

transmittance (T(λ)) has been set to 0.5 for 420 nm filter on the 410–430 nm band, and to 1 for the other filters in their respective band-width.

Fig. 9 shows the expected signal rate in DN ms^{-1} as a function of the boresight latitude varying the position of the spacecraft in its orbit around the planet, for colours and panchromatic (PAN) filters (left-hand side plots and right-hand side plots, respectively). The dark current contribution has been taken into account, whose values have been obtained, as a function of the integration time, in Leonardo S.p.A. at nominal temperature T = 268 K with Repetition Time of 2 s. The expected flux was obtained for three different configuration of true anomaly (140°, 179°, 220°). The middle panels represent also the expected signal obtained without taking into account the dark current (dashed lines), in order to compare our results with the preliminary signal and the integration time evaluations of Da Deppo et al. (2016).

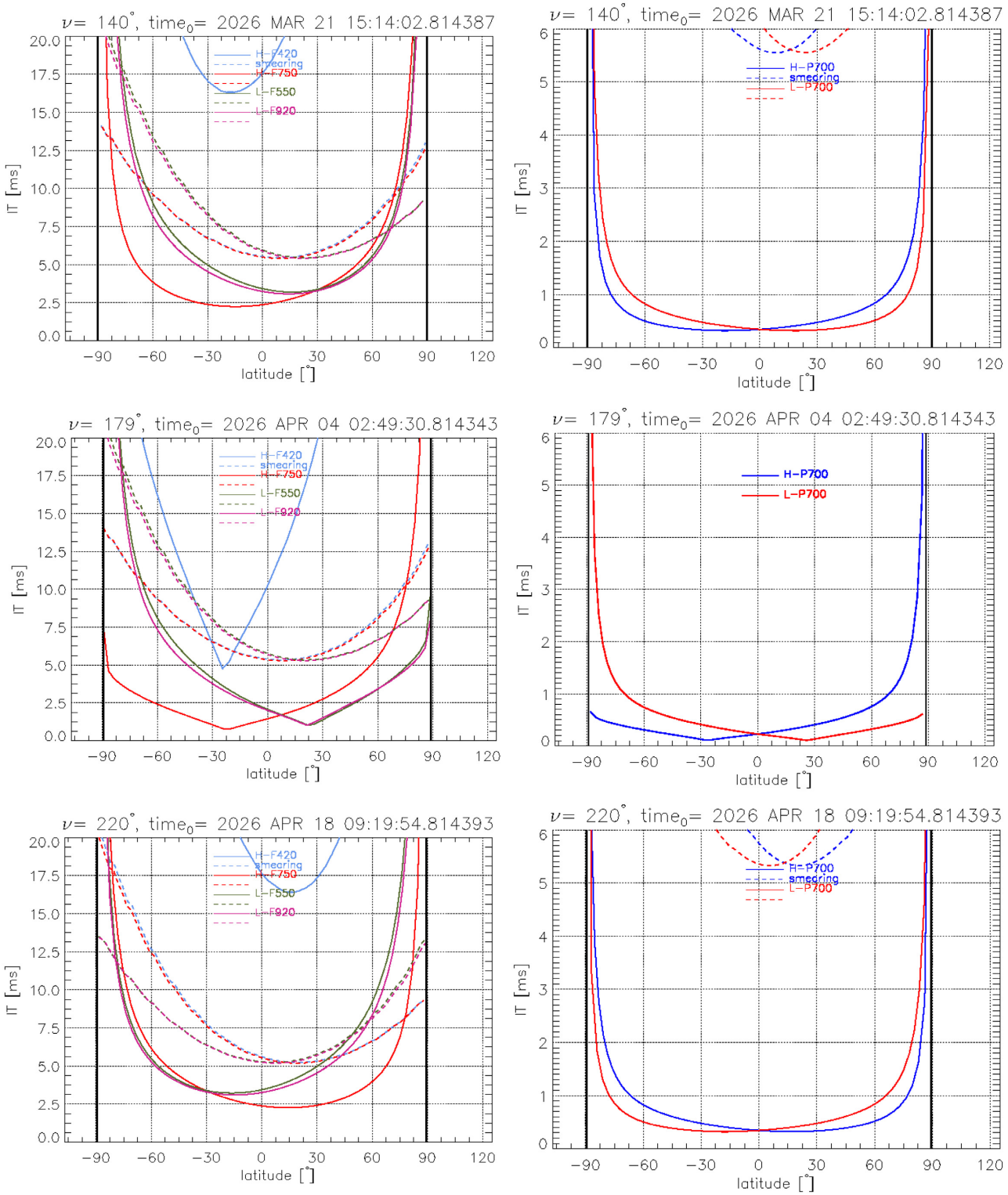

Figure 10. Expected integration times (IT) for STC. Integration times (IT) for colour and PAN filters (on left-hand and right-hand side of the panel respectively) as function of the latitude, for three different values of true anomaly, are shown. The dashed coloured lines represent the smearing time at 1/4 px. For PAN filters the smearing has not been included because it is out of the y-axis range. For the integration time calculation, the contribution of the dark current (DC) measured in Leonardo S.p.A. at nominal temperature (T = 268 K) and Repetition Time of 2 s have been taken into account.

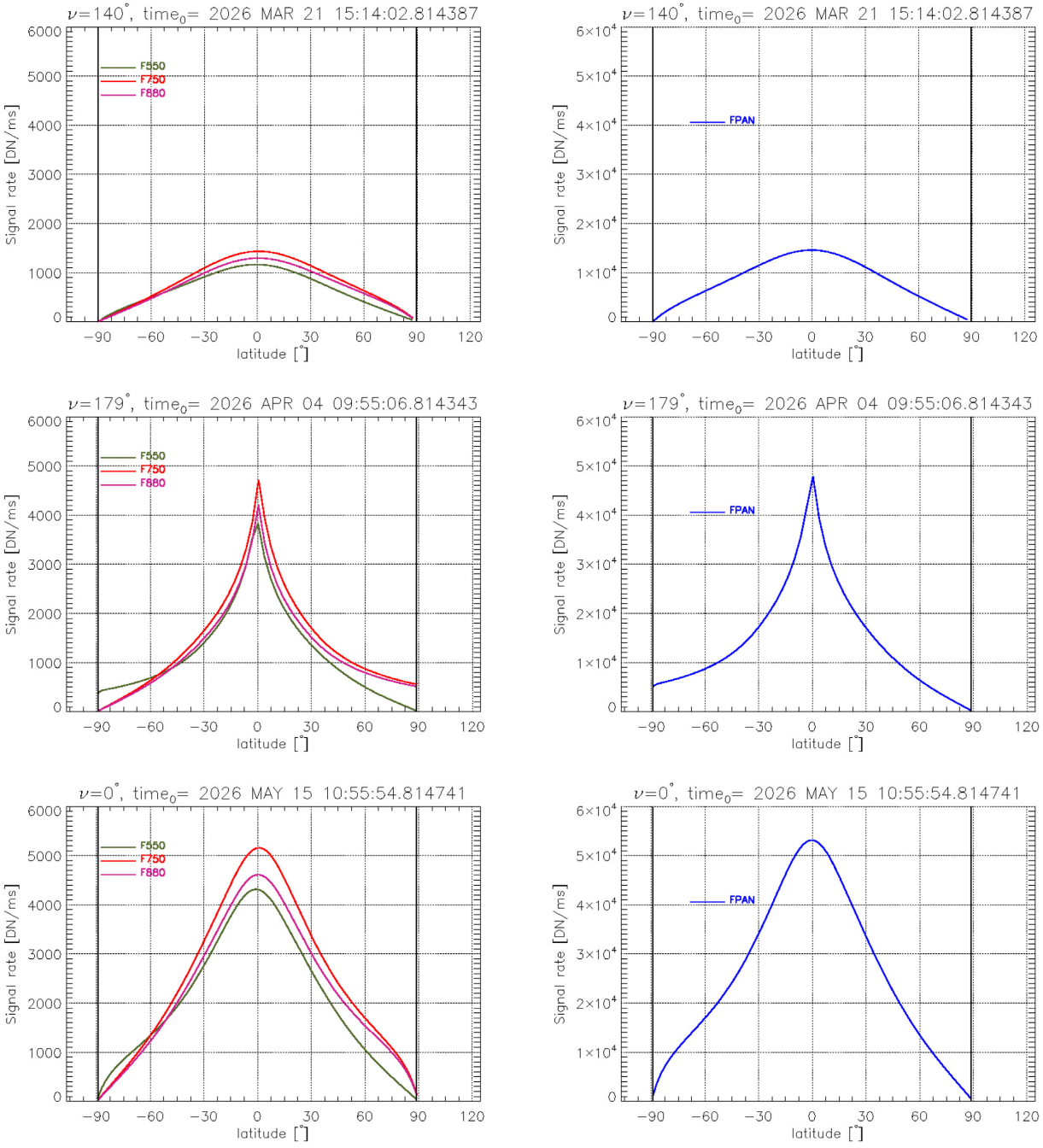

Figure 11. Signal rate in DN ms^{-1} expected for HRIC, calculated for colour filters (left-hand side column) and panchromatic (PAN) filter (right-hand side column) as a function of the boresight latitude. The results are obtained for different values of true anomaly. The variable time$_0$ is the absolute time correspondent to the spacecraft passage over the zero latitude. The results here reported have been obtained considering as dark current the values measured at Leonardo S.p.A. laboratories at nominal operating temperature (T = 268 K).

As expected, the curves relative to the signal rate of sub-channels H and L reach their maximum values for two different values of spacecraft subnadiral latitude. This result is a consequence of different line of sight of the sub-channel H and L for a specific position of the spacecraft with respect to Mercury (Fig. 7).

Further interesting considerations deriving from Fig. 9 concern the significant reduction of the maximum expected signal rate and the shape of the signal rate curve for true anomaly values different from $\nu = 180^\circ$ (middle panel of both figures). This effect is explained considering that, far from the apides, the incidence, emission, and phase angles sit in three different planes. As a consequence, the phase angle is not exactly the algebraic sum of incidence and emission angle. This results in a smooth increase of the phase angle with the increasing latitude and, hence, a smooth decrease of the hermean reflectance.

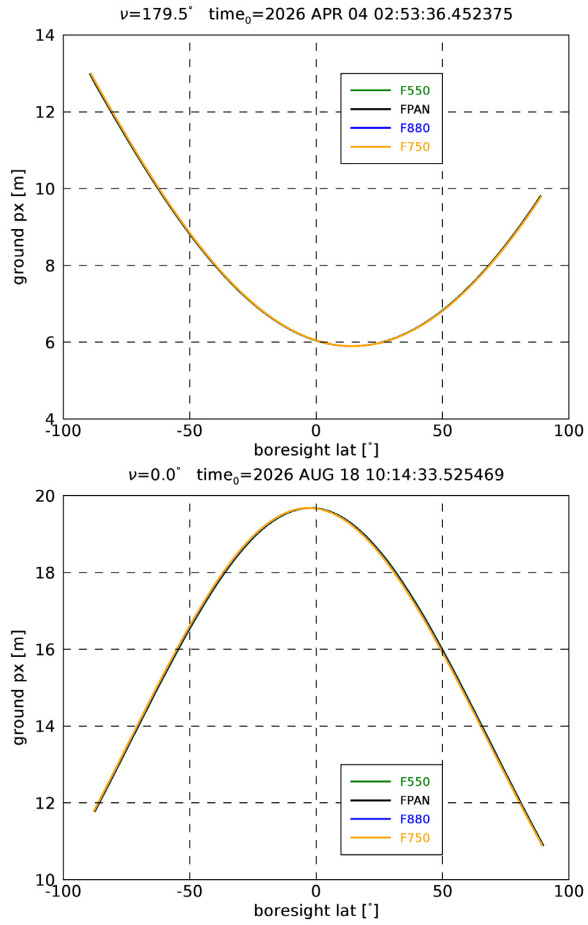

Figure 12. On-ground HRIC resolution as a function of boresight latitude, for all the filters. The plot on the top shows the result for the MPO orbit at aphelion, while the bottom plot is relative to perihelion.

When Mercury is at aphelion the spacecraft orbit sits in the plane that contains the Sun. In this configuration the illumination angles (i, e, α) sit in the same plane, thus the phase angle is exactly the sum of incidence and emission. When the spacecraft is near the zero latitude the phase angle reaches the minimum possible value, which lead to obtain the maximum value of reflectance.

From the comparison between values obtained for $\nu = 180°$ and lat $= 0°$ and those derived by Da Deppo et al. (2016), it results that the present estimation of expected signal is 20 per cent higher. On the contrary, on the 420 nm filter our value is 30 per cent lower (Slemer et al. 2018). These differences are mostly due to the reflectance model used, which gives different values of radiance. Furthermore, the preliminary calculations computed by Da Deppo et al. (2016) include some approximation related to the instrument and orbit configuration: the major axis of the spacecraft orbit sits in the equatorial plane (so that the periherm is above the subnadiral latitude), and the stereo configuration of the STC has not been taken into account.

Using the SIMBIOSYS simulator also the integration time needed to avoid the detector saturation can be calculated. It is derived by optimizing the signal dynamical level considering the detector full well capacity of about 90 ke$^-$. The integration times have been derived for each filter and are shown in Fig. 10, for colour and PAN filters, respectively. Dashed coloured lines show the smearing at 1/4 px. The results for Mercury at perihelion (panel with $\nu = 179.8°$) show that the values of the integration times obtained are underestimated by 30 per cent with respect to Da Deppo et al. (2010) (Slemer et al. 2018).

7.2 HRIC outputs

The simulator can be applied also to the HRIC channel given that its characteristics, i.e. the transmission properties (T(λ)), the filter transmissions (F(λ)), and the quantum efficiency of the detector (QE(λ)) are taken into consideration. The values of T(λ)), F(λ)), and QE(λ) taken into account are those obtained by Leonardo S.p.A..

Fig. 11 includes three couples of plots that show the estimation of signal rate of HRIC channel as a function of the boresight latitude (Slemer et al. 2018). Each couple shows the results for colour filters (left-hand side) and PAN filter (right-hand side) for different true anomalies (140°, 180°, and 0°).

Comparing the plots at different true anomaly, it is clear that the signal rate reaches higher values when Mercury is near the aphelion and near the perihelion. This effect, as previously explained, is due to the changing of the geometrical configuration of the illumination angles. At low illumination angles the SHOE affects the value of hermean reflectance. This effect has not been considered by Domingue et al. (2016) in the calculation of the Hapke's model parameters. Nevertheless, there are only two configurations in which the SHOE could actually change the reflectance calculation, which corresponds to the Mercury aphelion and perihelion and the spacecraft near the zero latitude. Since these two configurations correspond to a very small interval of time with respect to the duration of the entire mission, the SHOE can be ignored in the present analysis.

Furthermore, the shape of the signal rate curve calculated for the aphelion case is different from that derived in the perihelion case, which is smoothed and with a slightly higher maximum with respect to the case of $\nu = 180°$. The difference is due to both to the elliptic orbit of MPO and to the sampling of the simulator. The arc of the orbit that covers the illuminated part of Mercury at perihelion is the one containing the apoherm, where the spacecraft velocity is lower with respect to the arc containing the periherm. Since the sampling of the code is determined by dividing the MPO orbit period in equal parts, the arc of the orbit containing the apoherm is oversampled with respect to the other one and the shape of the signal rate curve is smoother.

Moreover, the on-ground pixel scale, which depends on the distance between the spacecraft and the planet surface, is lower at aphelion, as shown in Fig. 12. The two plots represent the on ground px dimension for all HRIC filters as a function of the boresight latitude, for aphelion (top plot) and perihelion (bottom plot). As expected, the on-ground resolution is better for $\nu = 180°$ than for $\nu = 0°$.

Fig. 13 shows the integration times as function of the boresight latitude for colour and PAN filters, for the same true anomalies considered in Fig. 11. The continuum line refers to the integration times, while the dotted line represents the smearing time at 1/4 px. We considered the binning factor of 1, so that the smearing time is considerably lower than the estimated integrated times. This result changes depending on the binning factor (2×2 or 3×3) considered.

7.3 VIHI outputs

The VIHI channel resolves 256 spectral bands with a spectral sampling of 6.25 nm band^{-1}, so that the signal rate has to be

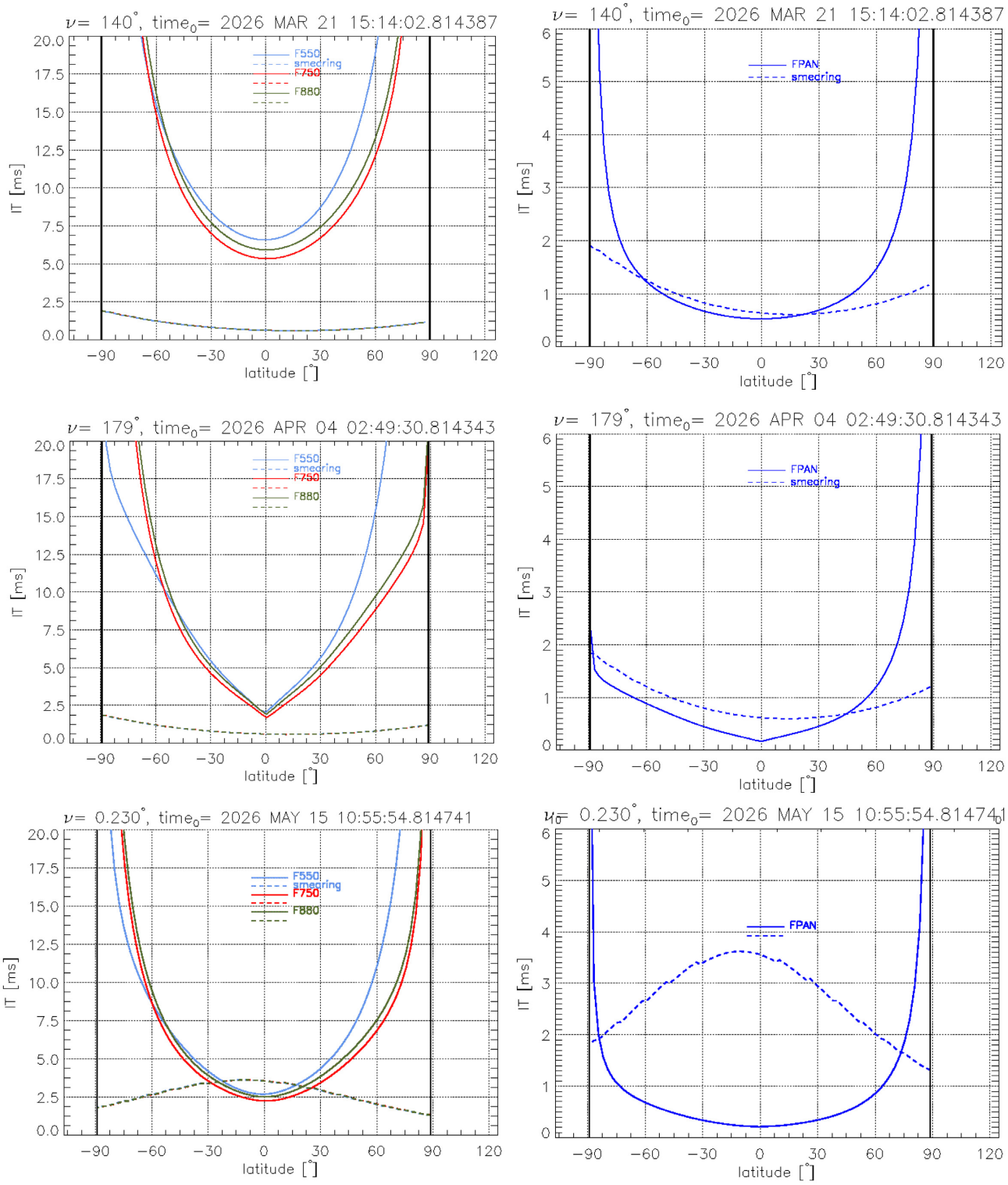

Figure 13. Expected integration times (IT) for HRIC as function of boresigth latitude. The continuum lines refer to Integration times of PAN and colour filters, while dashed lines refer to the smearing. The results are obtained for different values of true anomaly. The variable time_0 is the absolute time correspondent to the spacecraft passage over the zero latitude. The results here reported take into account the dark current measured at Leonardo S.p.A. laboratories at nominal operating temperature (T = 268 K).

calculated separately for each spectral band:

$$F(\lambda_i) = \int_{\Delta\lambda} B(\lambda_i) \cdot \frac{1}{\pi} \cdot R(\lambda_i) \cdot \rho(\lambda_i) \cdot \mathrm{d}\lambda_i. \qquad (11)$$

The term $B(\lambda)[W/(\mu m\, m^2\, sr)]$ represents the radiation coming from the Sun, calculated for the Mercury–Sun distance; the term $R(\lambda)$ stands for the hermean reflectivity derived using the Hapke's

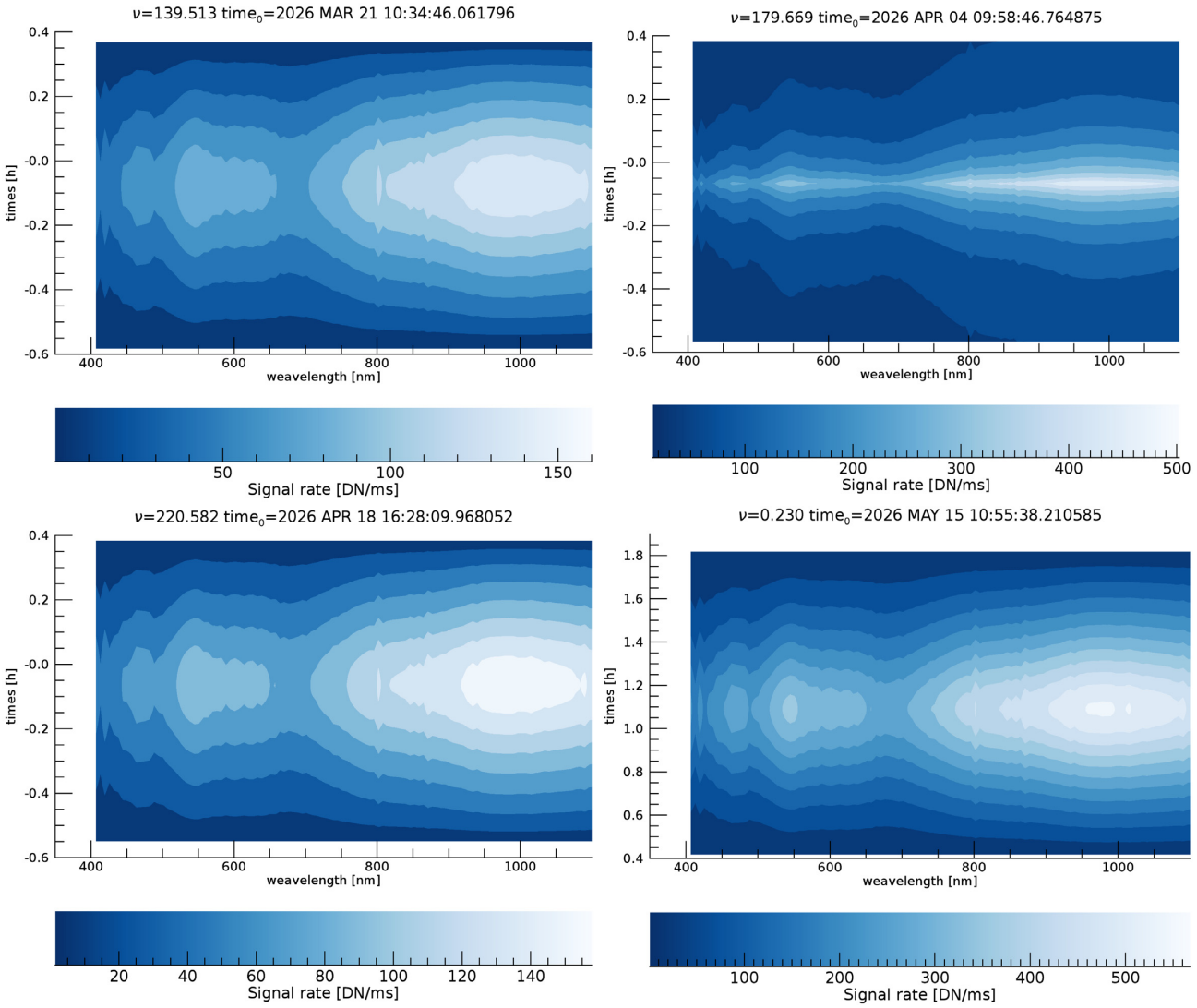

Figure 14. The VIHI expected signal rate detected in DN ms^{-1}, as function of the relative time and the wavelength. Different plots refer to different values of true anomaly.

model, and the $\rho(\lambda)$[DN $\mu\mu$m m^2 sr/(W s)] is VIHI channel responsivity (Filacchione et al. 2018a). The integral range $\Delta\lambda$ is 6.25 nm band^{-1}. Fig. 14 shows the signal rate as function of the wavelength and the relative time with respect to the periherm (*time*$_0$). Each plot refers to a different value of true anomaly. Due to the availability of the Hapke's model parameters, the simulations for the VIHI channel are restricted to the 400–1200 nm spectral range.

We considered four different dates in the first six months of observations. Some interesting considerations arise from the comparison between the four plots of Fig. 14:

(i) The variation of the signal rate as function of the relative time is smoothed for true anomalies far from the apsides, so that the signal rate measured decreases slowly with the boresight latitude. This effect, which is analogue to the behaviour described for STC and HRIC, is a consequence of the fact that the MPO orbit plane does not change during the mission, so that the illumination angles does not sit in the same plane for different true anomalies. Moreover, the weak difference observed between the perihelion and aphelion configuration is due to the different value of radiance incoming to the hermean surface, which scales with the square of the Sun–Mercury distance.

(ii) The maximum value of the signal rate is obtained for true anomalies near the apsides. Therefore, the best instrument performance will be reached near the aphelion and near the perihelion.

(iii) The tilt of the apsides line of MPO orbit with respect to the equatorial plane explains the position of the maximum value of the signal rate as a function of the subnadiral latitude. As expected, this position does not correspond to the zero-latitude because the periherm does not coincide with the point of zero boresight latitude. This effect is valid for the beginning of the mission because the periherm latitude decreases during the mission from 16° to −40° after 700 d from the beginning of science mission Jehn (2015).

Using the signal rate in DN ms^{-1} shown in Fig. 14, it is possible to derive the integration times needed to reach the full well capacity of the detector, which has been given by Raytheon Vision System and is 2 Me$^-$ (corresponding to 13 200 DN after signal digitalization; Altieri et al. 2017; Filacchione et al. 2018b).

Fig. 15 shows the integration times derived from the simulator here presented, as a function of the wavelength and relative time.

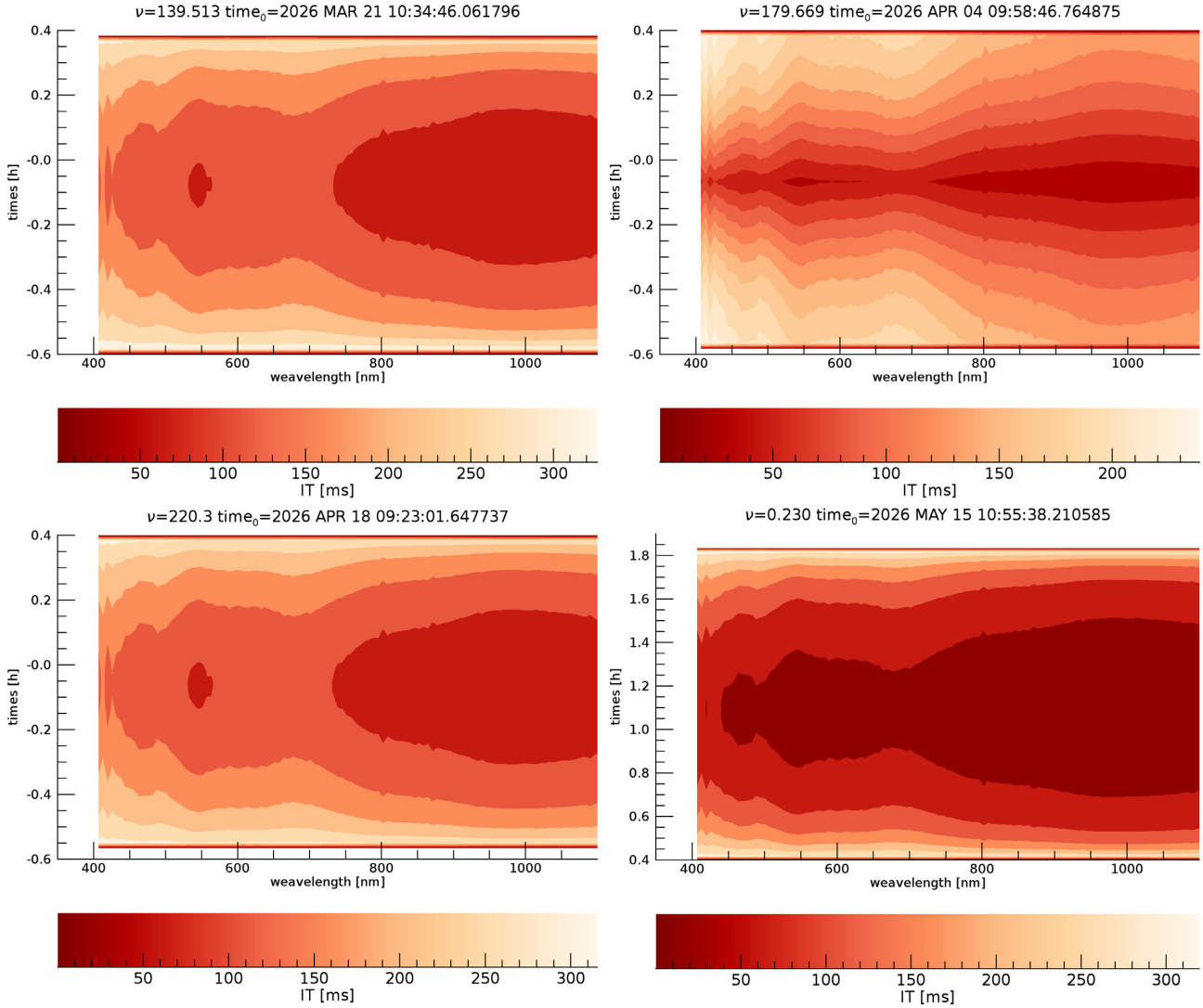

Figure 15. The VIHI expected integration time (IT) in ms as function of the wavelength and the relative time of observation. Different plots are relative to different values of true anomaly.

8 CONCLUSIONS

This work describes the simulator developed for the SIMBIOSYS instrument of the Mercury Planetary Orbiter spacecraft. The simulator includes a SPICE kernels based code used to predict the instrument performance and to determine some useful quantities related to the observation such as the repetition time and the integration time.

The simulator also includes the radiometric model of SIMBIOSYS instrument, which is derived starting from the Hapke's reflectance model. The radiometric model allows us to estimate the expected signal rate in DN ms^{-1} detected by each SIMBIOSYS channel during the entire mission by knowing the position of Mercury and orientation of the spacecraft. Once the values of the signal rate are known, the integration times needed to avoid the detector saturation and the image smearing can be derived.

Nevertheless, other outputs have been derived from the simulator, such as position, velocity, altitude with respect to the planet surface, and other properties characteristics of each instrument (expected footprints of the filters of the camera, the geometrical smearing, the integration time for each SIMBIOSYS sub-channel, and the expected signal to noise ratio reached).

The SIMBIOSYS simulator is a useful tool not only for the determination of the instrument performance but also for defining the in-flight calibration and, more important, the observation planning during the science mission phase at Mercury.

In this context, the simulator has been applied for the first time during the Near Earth Commissioning Phase (NECP). The simulator outputs are fundamental to prepare a specific operation test with all the three SIMBIOSYS channels working together (inter-channels test) during a nominal one orbit period at Mercury.

ACKNOWLEDGEMENTS

This work has been financed by the BepiColombo Agenzia Spaziale Italiana (ASI) contracts to the Istituto Nazionale di Astrofisica (I/022/1070 and 2017-47-H.0) and with the support of Leonardo Company S.p.A. (Campi di Bisenzio (FI) – Italy).

REFERENCES

Acton C., Bachman N., Elson L., Semenov B., Turner F., Wright E., 2005, SpaceOps 2002 Conference. p. 31

Altieri F. et al., 2017, Rev. Sci. Instrum., 88, 094503

Benkhoff J. et al., 2010, Planet. Space Sci., 58, 2

Blewett D. T., Robinson M. S., Denevi B. W., Gillis-Davis J. J., Head J. W., Solomon S. C., Holsclaw G. M., McClintock W. E., 2009, Earth Planet. Sci. Lett., 285, 272

Capaccioni F. et al., 2010, IEEE Trans. Geosci. Remote Sens., 48, 3932

da Deppo V., Naletto G., Cremonese G., Calamai L., 2010, Appl. Opt., 49, 2910

da Deppo V., Martellato E., Simioni E., Naletto G., Cremonese G., 2016, in Angeli G. Z., Dierickx P., eds, Proc. SPIE Conf. Ser. Vol. 9911, Modeling, Systems Engineering, and Project Management for Astronomy VI. SPIE, Bellingham, p. 99111T

Domingue D. L., Murchie S. L., Denevi B. W., Ernst C. M., Chabot N. L., 2015, Icarus, 257, 477

Domingue D. L., Denevi B. W., Murchie S. L., Hash C. D., 2016, Icarus, 268, 172

Filacchione G. et al., 2018a, 5th IEEE International Workshop on Metrology for AeroSpace (MetroAeroSpace). p. 252

Filacchione G. et al., 2018b, 5th IEEE International Workshop on Metrology for AeroSpace (MetroAeroSpace). p. 252

Flamini E. et al., 2010, Planet. Space Sci., 58, 125

Hapke B., 2002, Icarus, 157, 523

Hapke B., 2012, Icarus, 221, 1079

Hapke B., Denevi B., Sato H., Braden S., Robinson M., 2012, J. Geophys. Res., 117, E00H15

Hawkins S. E. et al., 2007, Space Sci. Rev., 131, 247

Jehn R., 2015, MAS Working Paper, 525, 1

Mills R. E., Drab J. J., Gin A., 2009, in Warren P. G., Marshall C. J., Heaney J. B., Kvamme E. T., Tyson R. K., Hart M., eds, Proc. SPIE Conf. Ser. Vol. 7439, Astronomical and Space Optical Systems. SPIE, Bellingham, p. 74390A

Murray B. C., 1975, J. Geophys. Res., 80, 2342

Schulz R., Benkhoff J., 2006, Adv. Space Res., 38, 572

Simioni E., De Sio A., Da Deppo V., Naletto G., Cremonese G., 2017, Proc. SPIE Conf. Ser. Vol. 1056, CMOS Detectors: Lessons Learned during the STC Stereo Channel Preflight Calibration. SPIE, Bellingham, p. 105622M

Simioni E. et al., 2019, Rev. Sci. Instr., 90, 043106

Slemer A. et al., 2018, Proc. SPIE Conf. Ser. Vol. 10698, Space Telescopes and Instrumentation 2018: Optical, Infrared, and Millimeter Wave. SPIE, Bellingham, p. 106984C

Slemer A. et al., 2019a, Measurement, 135, 828

Slemer A. et al., 2019b, Proc. SPIE Conf. Ser. Vol. 11180, International Conference on Space Optics — ICSO 2018. SPIE, Bellingham, 111807R

Zusi M., Paolinetti R., Della Corte V., Marra G., Baroni M., Palumbo P., Cremonese G., 2019, Appl. Optics, 58, 4059

APPENDIX:

As defined in Section 5.2.1, the Hapke reflectance model depends by both the geometrical and morphological properties of the Hermean surface. The geometrical properties can be summarized in the Henyey–Greensten function, given by:

$$p(\alpha) = \frac{(1-c)(1-b^2)}{(1-2b\cos(\alpha)+b^2)^{3/2}} + \frac{c(1-b^2)}{(1-2b\cos(\alpha)+b^2)^{3/2}}, \quad \text{(A1)}$$

where the parameter c is the partition between forward and backward scattering, and b is the amplitude of the scattering component.

The surface properties has been defined by the large-scale roughness $\sigma(i, e, \alpha, \theta)$, which depends by the scattering angles and by the surface roughness expression θ:

$$\sigma(i,e,\alpha,\theta) = \frac{\mu_e}{\mu_0(e)}\frac{\eta_0}{\eta_{0e}(i)}\frac{\chi(\theta)}{1-f(\psi)+f(\psi)\chi(\theta)[\mu_0/\mu_{0e}(i)]}, \quad \text{(A2)}$$

where θ is a measure of the average surface tilt or surface roughness and ψ is the azimuth angle. The term μ_{0e} and μ_e are given by:

$$\mu_{0e} = \chi(\theta)\left[\cos(i)+\sin(i)\cos(\theta) \times \frac{\cos(\psi)E_2(e)+\sin^2(\psi/2)E_2(i)}{2-E_1(e)-(\psi/\pi)E_1(i)}\right] \quad \text{(A3)}$$

and

$$\mu_e = \chi(\theta)\left[\cos(e)+\sin(e)\tan(\theta)\frac{E_2(e)-\sin^2(\psi/2)E_2(i)}{2-E_1(e)-(\psi/\pi)E_1(i)}\right]. \quad \text{(A4)}$$

The equations (A2), (A3), and (A4) refers to the case with i < e. When the incident angle is higher than the emission one, the last three equations become:

$$\sigma(i,e,\alpha,\theta) = \frac{\mu_e}{\mu_0(e)}\frac{\eta_0}{\eta_{0e}(i)}\frac{\chi(\theta)}{1-f(\psi)+f(\psi)\chi(\theta)[\mu_0/\mu_{0e}(e)]}, \quad \text{(A5)}$$

$$\mu_{0e} = \chi(\theta)\left[\cos(i)+\sin(i)\cos(\theta) \times \frac{\cos(\psi)E_2(i)+\sin^2(\psi/2)E_2(e)}{2-E_1(e)-(\psi/\pi)E_1(i)}\right]. \quad \text{(A6)}$$

and

$$\mu_e = \chi(\theta)\left[\cos(e)+\sin(e)\tan(\theta)\frac{E_2(i)-\sin^2(\psi/2)E_2(e)}{2-E_1(e)-(\psi/\pi)E_1(i)}\right]. \quad \text{(A7)}$$

The sub-functions are defined as follows:

$$\chi(\theta) = \frac{1}{(1+\pi\tan^2(\theta))^{1/2}}, \quad \text{(A8)}$$

$$\eta_{0e}(i) = \chi(\theta)\left[\cos(i)+\sin(i)\tan(\theta)\frac{E_2(i)}{2-E-1(i)}\right], \quad \text{(A9)}$$

$$\eta_e(e) = \chi(\theta)\left[\cos(e)+\sin(e)\tan(\theta)\frac{E_2(e)}{2-E_1(e)}\right], \quad \text{(A10)}$$

$$E_1(x) = exp\left[-\frac{2}{\pi}\cot(\theta)\cot(x)\right], \quad \text{(A11)}$$

$$E_2(x) = exp\left[-\frac{1}{\pi}\cot^2(\theta)\cot^2(x)\right], \quad \text{(A12)}$$

$$f(\psi) = exp\left[-2\frac{\psi}{2}\right], \quad \text{(A13)}$$

and

$$\cos(\psi) = \frac{\cos(\alpha)-\cos(i)\cos(e)}{\sin(i)\sin(e)}. \quad \text{(A14)}$$

The terms different from the scattering angles are the parameters of the Hapke's reflectance function, which are summarized in Table A1.

For more detailed description see Hapke (2012), Hapke et al. (2012), and Domingue et al. (2016).

Table A1. parameter of the Hapke reflectance model Hapke (2012).

Parameter	Values range	Definition
Single scattering albedo (w)	from 0 to 1	Ratio of the amount of light scattered to the amount of light both scattered and absorbed
Single-particle scattering function amplitude (b)	from −1 to 1	Parameter that defines the amplitude of forward and backward scattering
Single-particle scattering function partition coefficient (c)	from −1 to 1	Parameters that affects the partition scattered light info forward and backward direction
Filling factor (ϕ)	from 0 to 0.75	Fraction of the regolith volume occupied by grains
SHOE amplitude B_{S0})	from 0 to 1	Amplitude of the effect due to shadow-hiding mechanism
SHOE width (h_S)	from 0.02 to 1.8 Domingue et al. (2016)	Width of the opposition effect due to shadow-hiding effect
CBOE amplitude (B_{CO})	from 0 to 1	Amplitude of the opposition effect due to coherent backscattering
CBOE width (h_c)	from 1.5 to 0 Domingue et al. (2016)	Width of the opposition effect due to coherent backscatter
Surface roughness (θ)	from 0° to 40°	Mean slope angle

This paper has been typeset from a TEX/LATEX file prepared by the author.